Classification of EMI Discharge Sources Using Time-Frequency Features and Multi-Class Support Vector Machine

Imene Mitiche*, Gordon Morison, Alan Nesbitt, Michael Hughes-Narborough[1],

Glasgow Caledonian University

Brian G. Stewart[2],

University of Strathclyde

Philip Boreham[3],

Doble Engineering

Abstract

This paper introduces the first application of feature extraction and machine learning to Electromagnetic Interference (EMI) signals for discharge sources classification in high voltage power generating plants. This work presents an investigation on signals that represent different discharge sources, which are measured using EMI techniques from operating electrical machines within power plant. The analysis involves Time-Frequency image calculation of EMI signals using General Linear Chirplet Analysis (GLCT) which reveals both time and frequency varying characteristics. Histograms of uniform Local Binary Patterns (LBP) are implemented as a feature reduction and extraction technique for the classification of discharge sources using Multi-Class Support Vector Machine (MCSVM). The novelty that this paper introduces is the combination of GLCT and LBP applications to develop a new feature extraction algorithm applied to EMI signals classification. The proposed algorithm is demonstrated to be successful with excellent classification accuracy being achieved. For the first time, this work transfers expert's knowledge on EMI faults to an intelligent system which could potentially be exploited to develop an automatic condition monitoring system.

*Corresponding author

Email address: imene.mitiche@gcu.ac.uk (Imene Mitiche)

[1]School of Engineering and Built Environment, Glasgow Caledonian University, G4 0BA, United Kingdom

[2]Institute of Energy and Environment, University of Strathclyde, 204 George Street, Glasgow G1 1XW, United Kingdom

[3]Innovation Centre for Online Systems, 7 Townsend Business Park, Bere Regis BH20 7LA, United Kingdom

Keywords: EMI, Partial Discharge, GLCT, uniform LBP, Multi-Class Support Vector Machine, classification accuracy, intelligent system, experts system.

1. Introduction

Failure of electrical insulation is the cause of 60% of electrical assets breakdown in high voltage power plants [1]. This includes generators, motors, transformers, switchgear and Isolated-Phase Buses (IPB). When faults develop in an insulation or a conduction medium in one of these assets, both radiated and conducted Electromagnetic Interference (EMI) or Radio Frequency Interference (RFI) may be produced from discharge sources such as Partial Discharge (PD), corona and arcing. PD is a common insulation diagnostic tool used to assess the condition of power plant assets while in operation [2]. PD is a discharge transfer that occurs as a sign of insulation degradation and is generally considered harmful for an asset as once present it becomes a further source of accelerated insulation degradation [3]. Corona is considered as a type of PD [4]. Arcing is a significant current flow that could be due to a broken conductor, loose connection or a sparking shaft grounding brush [5]. Analysis of EMI signals may be exploited to gain information on the power plant asset condition [5] and may help in early fault detection enabling further actions to be taken on the operating assets, whether for repair or shut down in extreme cases. This benefits plant owners in relation to safety enhancement, low maintenance or replacement cost, and reduced system's down time. Overall, it enables power plant companies to maximise return of investment, revenue and business profits.

A literature review on PD detection techniques was presented in recent papers [6] [7] and [8]. The summary of these papers includes a comparison of PD measurement methods and covers a large number of feature extraction and classification techniques. PD measurement and detection has received an increased attention in the past 20 years from both research and industry, where it was used for condition monitoring of insulation failure in electrical and mechanical machines [6]. The most popular PD measurement techniques can be classified in three main categories: electrical [9] [10], acoustic [11, 12, 13], Ultra-High-Frequency (UHF) [14] [15] and EMI [5] [16, 17, 18]. These techniques aim to capture the physical radiated phenomena due to PD activity. The-state-of-the-art approach of PD monitoring exploits pattern recognition and classification algorithms.

Past work demonstrated successful classification of simulated or experimental PD sources. For instance, pattern recognition was introduced in [19] to classify different cavity sizes in PD measured using the electrical method. The feature extraction approach was to retrieve characteristics (e.g., charge transfer, rise and fall time, pulse width etc.) related to PD pulse shape. Fuzzy logic decision tree was used for classification achieving adequate classification accuracy.

In [20] UHF PD signals were measured on an experimental set-up. Statistical and energy features-based were then extracted from the Time-Frequency (TF) dual-tree Complex Wavelet Transform (CWT) coefficients of the signals. Then, Radial Base Function (RBF) neural network was used for pattern recognition, however the classification accuracy results were considered moderately good. Similar work was performed in [21] on PD signals measured using UHF method, where higher order statistics features were computed on wavelet packet coefficients of PD signals as features. The authors employed probabilistic neural network was employed to classify different PD types including corona, floating, internal and surface PD and achieved a successful classification rate.

Recently, authors in [22] studied the classification of PD types, measured using the acoustic method, in a noisy High-Voltage (HV) environment. They employed as features the low-frequency components, obtained from the frequency spectrum using Fast Fourier Transform, of PD signals. The classification process was performed using a collection of 8 different algorithms, among them Support Vector Machine (SVM), where high performance was demonstrated.

The literature demonstrates that PD sources can be classified using pattern recognition technique, particularly using TF features and machine learning algorithms. Although EMI technique for PD measurement has been used since 1980 until the present [23], few work proposed classification and pattern recognition of EMI sources including PD [16] [24].

EMI testing is a method used to detect insulation degradation and conductor related faults in high voltage machinery found in power industry [5]. EMI Data is collected while the apparatus is operational. Advantages of EMI testing have been reported as follows. While previous PD measurement techniques have the ability to detect presence of PD, EMI signals can provide test engineers with the ability to identify other types of discharges (e.g. arcing) in addition to PD [25]. While results of PD analysis techniques may be affected the choice of test equipment, EMI testing provides accurate measurement since it employs detectors and preselectors that suppress overload and gain compression produced by high amplitude impulse noise [26].

Traditionally, experts in EMI investigate the data through audio spectrum analysis in order to identify any occurring defect [16]. However, this method can be time consuming for large data sets as it is performed manually. Moreover, it is not practical for online continuous monitoring. Inspired by this expert knowledge, this work aims to develop an automatic condition monitoring approach based on classification of different EMI discharge sources, also referred to as events, using feature extraction and machine learning techniques. The EMI technique has been successfully adopted, for many years, to detect faults occurring in generators and transformers (e.g. [27] [17] [5]). The difference between EMI and other fault detection techniques is that EMI uses both frequency and time domains of the collected signals employing the methods in the CISPR 16 Standard [28]. The EMI method uses a number of different bandpass filters over various frequency ranges for signal energy measurement. The acquisition of different frequency bands in a CISPR 16 spectrum indicates the presence of faults, with significant fault frequency bands less than 100MHz (see [27] [17]

[5]). The audio signal associated to the selected frequency of interest in the EMI spectrum is usually investigated and evaluated by EMI experts for "expert "-based fault classification such as corona, PD, arc, exciter pulses etc. [18]. To the authors knowledge, this paper presents the first EMI fault classification, or pattern recognition, in power assets using intelligent methods. The signals employed in this paper were measured at three different high voltage power plants that were reported through EMI expert analysis to contain faults. It is important to extract relevant and hidden features that best characterise the event's unique pattern. It was reported in [20] that features extracted in the time domain are not suitable for PD due to the signal's non-stationary nature. The Short Time Fourier Transforms (STFT) were employed in [29] to retrieve the relevant time and frequency characteristics of experimental PD signals which were subsequently used to identify multiple PD sources. The General Linear Chirplet Transform (GLCT) is a TF analysis tool similar to STFT, however GLCT has the advantage of capturing the time and frequency varying characteristics with more robustness to noise [30]. Local Binary Pattern (LBP) approach was employed in [31] for music genre classification where LBP feature vectors were retrieved from the STFT image of audio signals. This approach was also used in acoustic scene classification [32] and was proven to be simple in computation, effective and robust in retrieving non-redundant information in image processing [33] [34]. Inspired by GLCT and LBP, this work presents the first extension and application of these two techniques for EMI signals classification, where GLCT provides the TF image of each signal from which signal features are extracted using the LBP technique. The feature vectors are then fed into a Multi-Class SVM (MCSVM) classifier in order to identify the multiple EMI events. The employed algorithms and data are discussed in more details later in the paper. This paper presents two novelties, first a newly developed feature extraction approach based on a combination of GLCT and LBP algorithms, and second EMI expert's knowledge is captured and transferred to an intelligent system which has the ability to identify the different EMI discharge sources. The combination of these two novelties results in a unique work in instrumentation and measurement. The next section describes the framework of EMI analysis proposed in this work and the expert's EMI diagnosis method. Section III defines the principles of the employed feature extraction algorithms. Section IV briefly defines the theory of MCSVM. Section V provides practical details of the apparatus and the collected EMI data. The application of the developed algorithm to EMI data and results are also presented in this section. Finally, Section VI outlines conclusions to this work and suggests future actions for industrial application.

2. EMI data analysis

2.1. Methodology

The data acquisition and application process is summarised in Figure 1. The approach involves the following steps: 1) signals are measured on sites using the

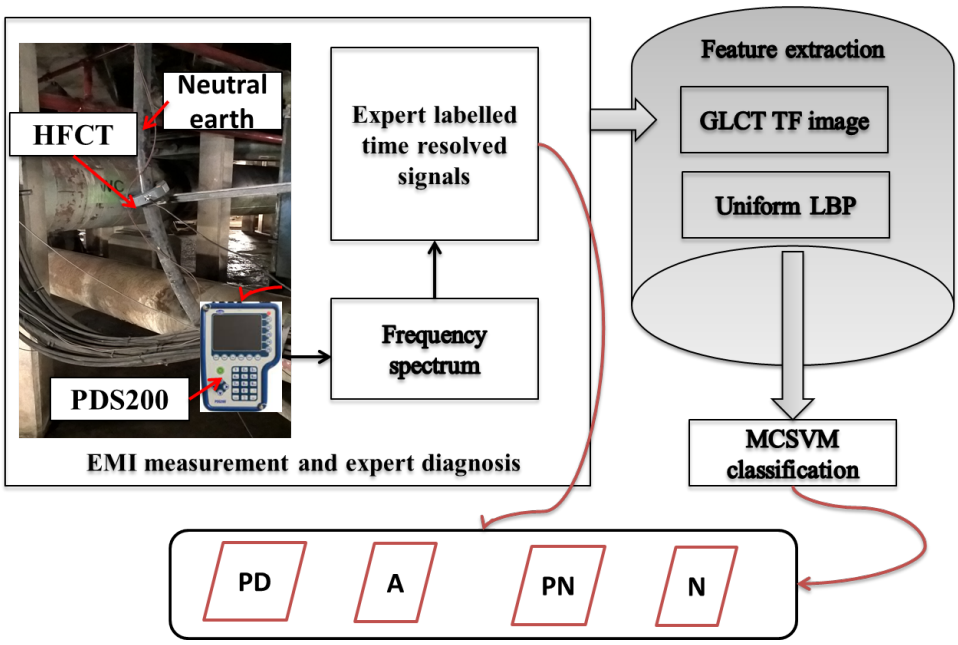

Figure 1: Framework of the proposed method for Electromagnetic Interference (EMI) analysis using High-Frequency Current Transformer (HFCT) and Partial Discharge (PD) Surveyor 200 (PDS200), discharge sources classification results are compared against experts' labelling of the sensed signals: PD, Arcing (A), Process Noise (PN) and Corona (C).

EMI technique providing the frequency spectrum from which experts select and label time resolved signals; 2) the time series are segmented into smaller signal chunks of 4000 samples for simple computation of the TF image and in order to feed the classifier with more instances for an improved training phase; 3) TF image of each segment is obtained using GLCT; 4) a histogram of uniform LBP is extracted as a feature vector of the TF image; 5) the feature vector is fed into the MCSVM classifier along with the relevant expert label.

2.2. EMI monitoring

Data measurement using the EMI method is performed as follows. Using a High-Frequency-Current-Transformer (HFCT), the signals are captured at a neutral earth of a generator or a transformer, following the method specified in the CISPR 16 (Committee International Special des Perturbations Radioelectriques) Standard [28]. CISPR 16 defines a quasi-peak detector implemented with different filter bandwidths over the range of frequencies to be measured. For instance, the B filter operates over 150kHz-30MHz, with a 6dB bandwidth of 9kHz, and the C filter from 30-300MHz with a 6dB bandwidth of 120kHz. The sampling time for quasi-peak detection is 1 second per selected frequency. In [5][27] [17] examples of measured EMI frequency spectrum are provided. This

allows capturing EMI time-domain signals at the frequencies of interest for audio analysis by EMI experts with the aim of identifying the event [18]. Such identification is based on previously accumulated experience of fault monitoring and forensic confirmation based on audio analysis. This approach is limited as it relies totally on the availability of experts with such knowledge. This paper attempts to overcome this limitation by using the expert's knowledge as a labelling method and a foundation to an intelligent pattern recognition algorithm for automatic fault classification of EMI time resolved data. The approach is to employ feature extraction and classification techniques which are described in the following section.

3. Feature Extraction algorithm

In this section the mathematical theory of GLCT and uniform LBP is presented.

3.1. General Linear Chirplet Transform (GLCT)

GLCT was proposed by Yu and Zhou to analyse time-varying Instantaneous Frequency (IF) signals and to overcome some limitations in STFT and the Linear Chirplet Transform (LCT) [30]. This includes higher energy concentration and better resolution on the T-F domain with reduced cross-term interference, superior ability to analyse non-linear single and multi-component signals, and finally more tolerance against noise [35].

The mathematical framework of GLCT is described as follows. First, denoted in Equation 1 is a time-varying IF signal with amplitude $A(t)$ and IF $\phi(t)$

$$x(t) = A(t).e^{i\int \phi(t)dt}. \tag{1}$$

Given a short time τ and an instantaneous time t', the IF can be a linear equation that is developed by Taylor expansion as follows.

$$\phi(\tau) = \phi(t') + \phi'(t')(\tau - t'). \tag{2}$$

By applying a short window $w(\tau - t')$ to $x(\tau)$ at $\phi(t')$, then calculating the FT of their product gives:

$$\begin{aligned} |S(\phi(t'))| &= |\int_{-\infty}^{+\infty} w(\tau - t').x(\tau).e^{-i\phi(t')\tau}d\tau|. \\ &= |\int_{-\infty}^{+\infty} w(\tau - t').A(\tau).e^{i\phi(t')\tau + i\phi'(t')(\tau - t')^2/2} \\ &.e^{-i\phi(t')\tau}d\tau|. \end{aligned} \tag{3}$$

By performing some mathematical manipulations, Equation 3 is simplified to obtain Equation 4.

$$|S(\phi(t'))| = |\int_{-\infty}^{+\infty} w(\tau - t').A(\tau)d\tau|. \tag{4}$$

It is observed that there is a modulated element $e^{i\phi'(t')(\tau-t')^2/2}$ which causes dispersion of the energy around IF and higher concentration of harmonics on the T-F domain. In order to remove the modulated element, a demodulated factor is introduced to the general STFT in Equation 5 to obtain the new formulation in Equation 6. The latter includes the chirp rate "c"space which aims to rotate the signal by a degree of $\arctan(c)$ in the TF space.

$$S(t',\omega) = \int_{-\infty}^{+\infty} w(\tau - t').x(\tau).e^{-i\omega\tau} d\tau. \tag{5}$$

$$S(t',\omega) = \int_{-\infty}^{+\infty} w(\tau - t').x(\tau).e^{-i\omega\tau}.e^{-ic(t')(\tau-t')^2/2} d\tau. \tag{6}$$

The new STFT amplitude can hence be calculated as follows.

$$\begin{aligned} |S(t',\phi(t'))| &= |\int_{-\infty}^{+\infty} w(\tau - t').x(\tau).e^{-i\phi(t')\tau} \\ &\quad .e^{-ic(t')(\tau-t')^2/2} d\tau| \\ &= |\int_{-\infty}^{+\infty} e^{i(\phi'(t')-c(t'))(\tau-t')^2/2} \\ &\quad .w(\tau - t').A(\tau) d\tau|. \end{aligned} \tag{7}$$

The inconvenience of this demodulated solution is that it is difficult to predefine the factor accurately because the IF characteristics of a signal cannot be estimated a priori. A possible approach is to employ a series of discrete demodulated factors to estimate the optimum factor given by:

$$S(t',\omega,c) = \int_{-\infty}^{+\infty} w(\tau - t').x(\tau).e^{-i\omega\tau}.e^{-ic(\tau-t')^2/2} d\tau. \tag{8}$$

This way, for each (t',ω) if the discrete factor corresponds to the modulated factor, then the T-F around the signal's IF will have high energy concentration and maximum amplitude. Thus based on this amplitude, the best parameter "c"can be calculated as:

$$c' = \underset{c}{argmax} |S(t',\omega,c)|. \tag{9}$$

Finally, GLCT can be computed as follows.

$$GS(t',\omega) = S(t',\omega,c'). \tag{10}$$

Note that Equation 8 is equal to LCT, when $c = 0$, from which GLCT (Equation 10) is derived. The demodulated factor results in a rotation on the TF by an angle of $\arctan(-c)$. This is characterised by a rotating parameter $\alpha \in [-\frac{\pi}{2}, \frac{\pi}{2}]$ which is defined in Equation 11 for a known sampling time T_s and frequency F_s of a signal.

$$\alpha = \arctan(\frac{2T_s}{F_s}.c) \tag{11}$$

Assume that α has N values which divide the T-F domain into N+1 segments evenly as:

$$\alpha = -\frac{\pi}{2} + \frac{\pi}{N+1}, -\frac{\pi}{2} + \frac{2\pi}{N+1} ..., -\frac{\pi}{2} + \frac{N\pi}{N+1}. \tag{12}$$

Then, this N parameter is what differentiates GLCT from STFT. However, when $N = 1$ then GLCT yields to STFT. The recommended N value by authors in [30] lies between 5 to 10. They demonstrated that higher values do not reduce errors or cross terms interference any further, however computation is increased which is not desired in signal processing implementations. An example non-stationary signal is provided in Figure 2 from which the TF image was calculated using STFT and GLCT algorithms as illustrated in Figures 3 and 4 respectively. It is observed that GLCT extracts the IF with better resolution and concentration than STFT.

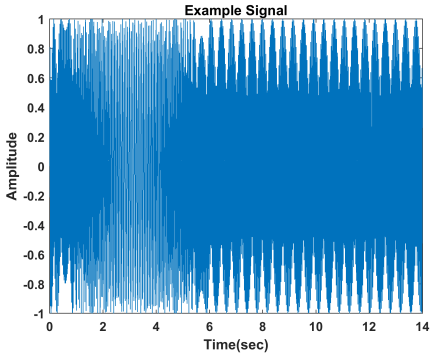

Figure 2: Example non-stationary Signal

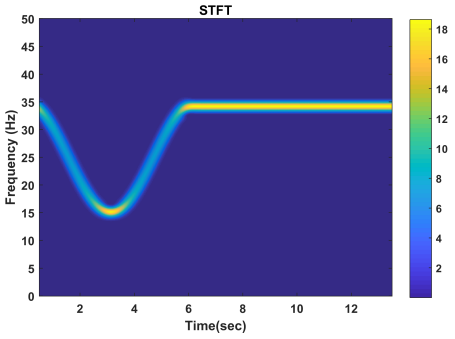

Figure 3: STFT image of the example non-stationary Signal

By treating the 2-D output of the GLCT as an image we can then employ image recognition technique to the 1-D time series. Specifically, we apply the Local Binary Pattern histogram [36].

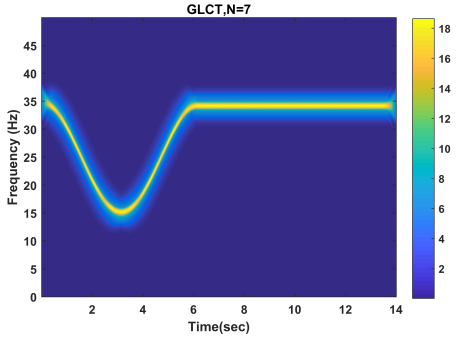

Figure 4: GLCT image of the example non-stationary Signal

3.2. Local Binary Pattern (LBP)

LBP exploits the image pixels by comparing their values to those of neighbouring ones and uses the result as binary number to labels each pixel [36]. Figure 5 illustrates an example which explains the mathematical concept of coding a 2-D image to LBP. Suppose that "C" is the centre pixel and "P" the neighbours equally spaced from "C" at distance "R" (see Figure 6), the joint difference distribution is calculated as:

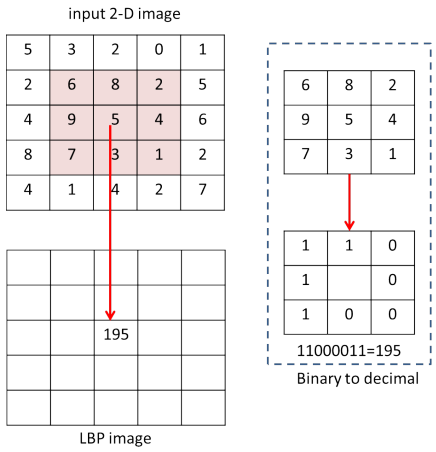

Figure 5: LBP image encoding of a 2-D image

$$T \approx (g_0 - g_C, ..., g_{P-1} - g_C) \tag{13}$$

where g_C and g_0 to g_{P-1} are the Gray level intensity of the centre pixel C and the neighbouring pixels P respectively. The sign of the difference is then used to denote:

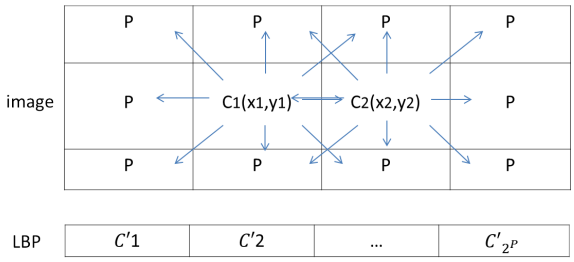

Figure 6: LBP histogram representation of an image

$$s(g_i - g_c) = \begin{cases} 1 & \text{if} \quad g_i \geq g_C \\ 0 & \text{if} \quad g_i < g_C \end{cases}$$

where T can be written in Gray scale format $T \approx (s(g_0 - g_C), ..., s(g_{P-1} - g_C))$, for the neighbours index $i = [0, P]$. Finally an LBP value for each pixel C, with the coordinates $(\mathrm{x}_C, \mathrm{y}_C); \mathrm{x}_C \in \{0, ..., N-1\}, \mathrm{y}_C \in \{0, ..., M-1\}$ on the NxM image, is calculated as follows:

$$LBP_{P,R}(\mathrm{x}_C, \mathrm{y}_C) = \sum_{i=0}^{P-1} s(g_i - g_C) 2^i. \tag{14}$$

This results in a unique value $0 \leq C' \leq 2^i$. A histogram with size P^2 of LBP values is created producing a vector of 256 descriptive features for 8 neighbours. Figure 6 illustrates how this is derived. It was recommended in [37] to consider only the possible uniform values in the histogram. They also suggested to implement LBP with 2 points distance. This implies a reduction of the feature vector dimension from 256 to 59 and improvement in computation. An LBP is uniform if the binary code has a maximum of two 01 or 10 transitions. For instance, the LBP in Figure 5 for example is uniform. A non uniform LBP would be 10010010. Non-uniform LBP descriptors are considered noisy and useless for classification, whereas the uniform ones provide information on uniform regions, edges and corners in the image [38]. This property could be exploited to extract such information from the TF behaviour of the discharge sources. A deeper explanation of uniform LBP can be found in [39]. Thus, uniform LBP with the parameters $R = 2$ and $P = 8$ neighbours are chosen in this work.

4. Support Vector Machine(SVM) and Multi-Class SVM(MCSVM)

SVM was introduced by Vapnik [40] in the early 90s as a regression and binary classification method which draws an optimum hyperplane that separates two classes of data having unique patterns. This method is exploited in different applications including text classification, sound recognition and image categorisation [41]. SVM is popular because it has the ability to deal with high-dimensional features whilst providing higher classification accuracy than the

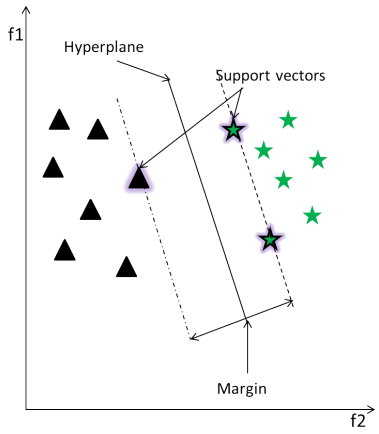

Figure 7: SVM linear separation

other algorithms such as neural networks, K-nearest neighbour, random forests and linear discriminant analysis [42]. Moreover, larger feature dimension can be implemented in SVM which may reduce confusion between the different classes and thus enhances classification accuracy. The hyperplane is obtained via a kernel function which can be linear, polynomial or Radial Basis Function (RBF). The feature space is obtained in two main steps for a dataset that includes features of two classes. First, SVM draws an optimal line that separates the two different data features, as illustrated in Figure 7, in that feature groups that represent the first class will be clustered on one side and the ones representing the second class will lie on the other side of the feature space. This produces the SVM model based on what is called the training phase. Second, SVM classifies unseen input data based on the trained model; this is called the testing or validation phase of SVM. The distance between the hyperplane and the nearest point of each class is called the margin. The width of the margin affects the SVM performance in that the larger margin the better the classification accuracy achieved. The separation is achieved through a kernel function which is usually chosen depending on the nature of the data. For instance, the linear function draws a line to separate the classes, whereas the RBF draws a circle to separate, then map the clusters to a linear plane as shown in Figure 8. The most used kernel function in SVM is the non-linear RBF because it has the advantage to map higher dimensional data than the linear function. In addition, it has low computational complexity and it requires less parameters than the polynomial function. Here, a grid search method [43] was performed in order to find the optimum kernel function along with its parameter to implement in SVM for the best results. This method involves several training and testing operations of the algorithm with all possible kernel functions and their parameters.By applying this technique, it was found that the best performance is achieved when using

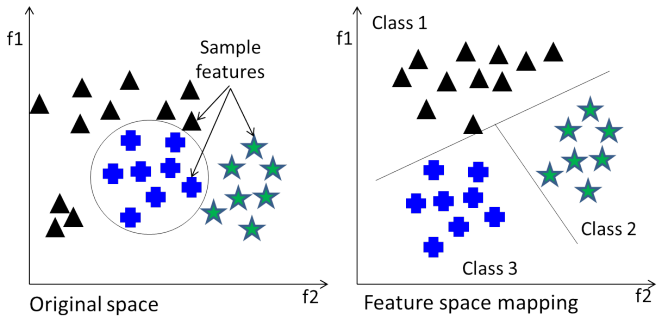

Figure 8: SVM linear space mapping using RBF kernel function

the RBF kernel, with $\sigma = 0.5$, which is defined as follows.

$$K(x_i, x_j) = e^{-\frac{||x_i - x_j||^2}{2\sigma^2}} \tag{15}$$

where σ is the width of the RBF function.

The mathematical theory of SVM can be described as follows: Let x_i be the data input and y_i the associated labels in that $i = 1, 2, ...L$ is the data sample number. Let's assume that the data points belong to two classes "1"and "-1". Each data point is put into a feature space which is separated by a hyperplane with the basic geometric equation:

$$f(x) = w.x + b = 0 \tag{16}$$

where b is a scalar and w is an L-dimensional vector which plays an important role in determining the hyperplane position. The hyperplane will pass by the origin if $b = 0$. Otherwise, the margin will be created or increased. Equation 17 defines the hyperplane of the first class and Equation 18 defines the hyperplane of the second one.

$$w.x + b = 1. \tag{17}$$

$$w.x + b = -1. \tag{18}$$

Through geometric manipulations, the distance between the two hyperplanes can be obtained as $\frac{2}{|w|}$. The margin width can be maximised by minimising $|w|$ which brings in the criteria: $w.x_i + b \geq 1$ and $w.x_i + b \geq -1$ for the first and second class respectively. This will ensure that the points from each class do not surpass the hyperplanes which are also called support vectors. The instances that fall on the hyperplanes are called support vectors. The hyperplane is calculated by solving the optimisation problem in Equation 19, while taking into consideration two main parameters: the noise slack variable ζ_i and the error penalty C.

$$min\frac{1}{2}||w||^2 + C\sum_{i=1}^{M}\zeta_i. \tag{19}$$

$$Subject\ to \begin{cases} y_i(w^T.x_i + b) \geq 1 - \zeta_i \\ \zeta_i \geq 0, \qquad\qquad i = 1, ..., M \end{cases}$$

where ζ_i defines the range to which the samples exceed the margin and C states the trade-off between classification error, which results from the training phase, and maximisation of the margin. Equation 19 is transferred to Lagrangian optimisation problem. Further details and explanation can be found in [44]. This inserts an α_i parameter which expresses w in solving Equation 19. The solution results in a non-linear decision function which is defined in Equation 20.

$$f(x) = sign(\sum_{i,j=1}^{M}\alpha_i y_i(x_i x_j) + b). \tag{20}$$

The challenges that can be faced by the SVM learning process with high dimension feature space are data over-fitting and computational errors. Over-fitting can be tackled by implementing a kernel function which performs a dot product of the feature space i.e. $K(x_i, x_j) = (\Phi^T(x_i).\Phi(x_j))$, where the definition of this function is presented in [40] . This is similar to the case of non-linear mapping as discussed earlier. A non-linear vector function $\Phi(x) = (\phi_1(x), ..., \phi_l(x))$ with feature space of dimension l is implemented and the decision function in Equation 20 is reformulated to:

$$f(x) = sign(\sum_{i,j=1}^{M}\alpha_i y_i(\Phi^T(x_i).\Phi(x_j)) + b). \tag{21}$$

SVM is a binary classifier which means it can deal with only two different classes. In this paper as we seek to classify more than two events. MCSVM is implemented to overcome this issue by employing the One-Against-One (OAO) approach where $k(k-1)/2$ models are built and each one is trained on two classes, p and q, as a normal binary classifier. The testing is performed using a "Max Win" voting approach. If the test instance is near the p^{th} class then the vote for this class is incremented by one. The test instance is classified in the class which obtains the highest vote [45].

5. Application

5.1. EMI data description

The signals were measured during the assets' operation by means of an HFCT which is clamped around the neutral earth cable of the asset in order to collect PD signals electromagnetically. The signals were recorded at a sampling rate of 24kHz using a PDS200 instrument which provides time series and

frequency measurements to the international standard CISPR16 for EMI filter types. The PDS200 is a PD surveyor device which detects and analyses Radio Frequency Interference (RFI) in addition to EMI radiations. The device provides the frequency spectrum of the captured signals using quasi-peak detector. The latter is fast enough to measure the discharges intensity, unlike other detectors (e.g. AM rms) used in RFI testing [27]. The PDS200 is a radio receiver which captures EMI radiations in the range of 0 to 100MHz. The selected frequency of interest within this span demodulates, by means of AM demodulation, the signal which is sampled at 24 kHz. The PDS200 looks at signals based on the CISPR16 bandwidths (e.g. 9kHz, 120kHz) and moves through the frequency spectrum making appropriate power filtered response measurements at each frequency. For time domain signals the instrument permits any frequency between 150kHz to 100MHz to be selected e.g. where the maximum envelope energy exists. It then makes a slower filtered response measurement which is sampled at 24kHz.The time resolved signal can be retrieved for further analysis from a selection of significant peaks in the frequency spectrum. Figure 9 illustrates an example of the frequency spectrum obtained from a generator by the PDS200 quasi-peak detection and Figure 10 shows an example time series signal which was retrieved at 7MHz, measured from the generator in microvolts.

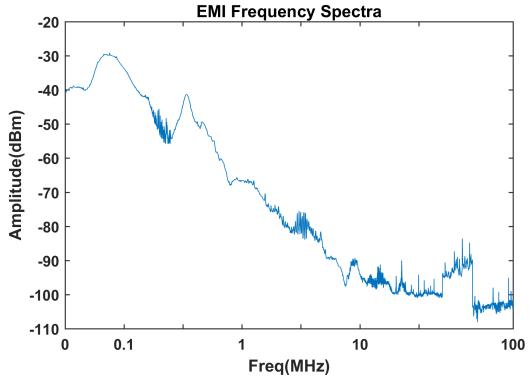

Figure 9: EMI frequency spectrum

Usually, the time signals are converted to audio format then examined by EMI experts in order to identify and label the discharge sources contained in the signals and comparing the signal to the audio signature for each fault type. These "expert"labels are used in training the classification algorithm. A number of signals were measured in 10 different sites from various assets. The focus in this work is to attempt the classification of signals that contain a single event per signal such as PD, arcing etc. In total, 7 single different events were labelled within the data. Each signal contains 500 cycles over a duration of 10 seconds. Table 2 presents the events and assets contained in each site and their notation is provided in Table 1. It is interesting to note that a minor event, such as the observed minor PD in the data, defines its presence with less repetition rate

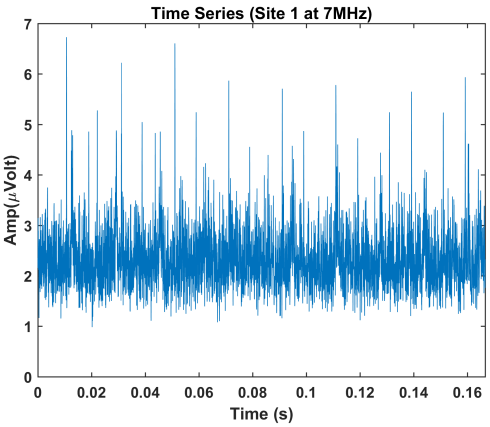

Figure 10: Time series signal captured at 7MHz

Table 1: faults' labels

Fault	Label
Arcing	**A**
Corona	**C**
Data Modulation	**D**
Exciter	**E**
minor Sparking	**mS**
Noise	**N**
Random Noise	**RN**
Partial Discharge	**PD**
Process Noise	**PN**

Table 2: Detected faults in each site

Site	Assets	Conditions
1	Unit 3 Background stair rail, Generator 2, Generator Unit 3, Unit 3 IPB Yellow Phase	PD, RN, PN, mPD, C, N
2	Generator Step-Up (GSU) 3, Gas Turbine 1 A/B/C Phase, Gas Turbine 2 A/B/C Phase, Gas Turbine 2 A Phase Coupler, Steam Turbine Generator A/B/C Phase, IPB, Station Transformer	PD, E, PN, D
3	Gas Turbine 2, IPB, Steam Turbine Generator	PD, E, PN
4	Boiler Feed Pump, Salt Water Pump, Steam Turbine Generator 3	mS, D, RN, PD, A
5	Generator, GSU	PD, E
6	Transformer 1B/2B	RN, D, PD
7	GSU 8	PD, PN, E
8	Unit (Auxiliary) Transformers 1a, 1b, 2a, and 2b	RN, D, E, PD, mS
9	Auxiliary Transformer, GSU, Steam Turbine Generator	PD, E
10	Generator Unit 1, 2 and 3	PN, E, PD

and reduced discharge level. The work in this paper is about classification not trending. However, once the fault is classified the PDS200 can permit trending [17] [46] to be undertaken e.g. repetition rate, magnitude level increases etc. so the severity can then be evaluated and trended. As the PDS200 measures selected frequencies using CISPR16 bandwidths the signals don't calibrate in the same way as conventional PD measurements.

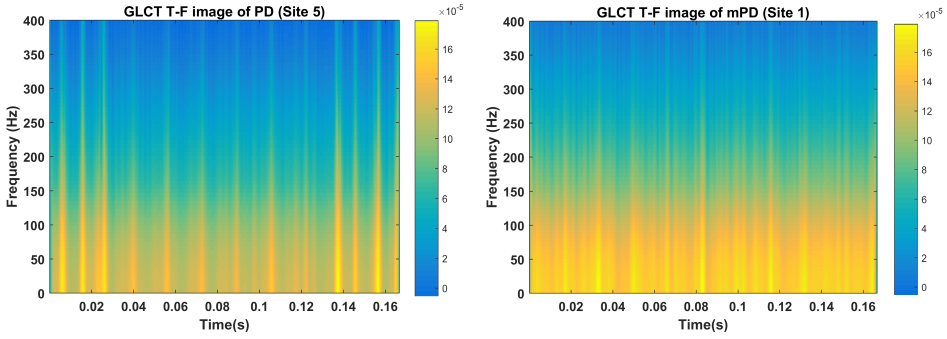

(a) (b)

Figure 11: TF image for (a) PD (b) minor PD.

5.2. Application and results

First, GLCT was calculated for each segment resulting in a TF image. Example GLCT TF images for (a)PD (b) mPD is shown in Figure 11. It is observed that these two events have different TF fingerprints and the visual distinction

between them is obvious. Similar differences are also observed between the different events, giving a motivation to use the GLCT image along with LBP as features to help event classification. In order to reduce the feature dimension and redundant information, uniform LBP with $R = 2$ and $P = 8$ was computed to extract the pattern of each TF image. This provided a total of 60 instances per signal with a feature vector length of 59. The feature vectors are then implemented in the MCSVM OAO algorithm for classification. The classifier is trained and tested using a ten-fold hold-on cross validation method where 10% of the total data set is kept for testing and the rest is used for training. A different data training/testing set is selected in ten iterations and the average of the resulting accuracies from each iteration is considered as the total classification accuracy. For results consistency, this simulation was performed several times with different N parameter values of the GLCT ($N = [1 - 15]$), where an improvement of only 1 to 2% in classification accuracy was obtained for $N \geq 3$.

5.3. Results

The classification performance is evaluated and presented in terms of accuracy percentage and confusion matrix. The latter aids to visualize the classification performance in terms of the true and predicted class of each event. Detailed explanation of the confusion matrix can be found in [47]. The classification was performed in two different scenarios as follows.

Table 3: Classification accuracy within each site

Site	**Classification Accuracy %**
1	81
2	100
3	100
4	96
5	100
6	98
7	100
8	98
9	100
10	100

5.3.1. Case 1

The MCSVM was trained and tested on each site using the ten fold cross-validation technique. Classification accuracy results within each site are presented in Table 3 which shows high classification accuracy for each site. A 100% accuracy was obtained in most sites (2, 3, 5, 7,9 and 10). Lower accuracy was obtained in each of the remaining sites. The lowest accuracy was observed in Site 1 (81%), yet this can be considered as good performance since the site contains 6 different events sensed from 4 different assets. It is noticed that sites

containing two or up to three events have the best classification accuracy. The latter is degraded as the number of events per site increases. In order to further investigate the results where accuracy of 100% was not achieved, confusion matrices between the different events were plotted in Figures 12 to 15 for Sites 1, 4, 6 and 8 respectively. Overall, classification confusions were observed between PD, mPD, RN and N in Site 1 (Figure 12). The major confusion was observed between mPD and PD with 44.4%. This could be because PD and mPD are the same fault type, thus a second stage analysis is required. For this concern, it may be possible to use other aspects of the signals to discriminate them and this is something which will be looked at in the future to improve classification. In Site 4 (Figure 13), PD has minor confusion (3.3%) with mS, A has small confusions with PD (1.4%) and mS (4.2%) and finally RN has small confusion with A (2.4%). In Site 6 (Figure 14), PD has confusion of 16.7% with RN and RN has a small confusion (3%) with D. Finally, only one confusion was observed in Site 8 (Figure 15) which is 2.8% between PD and mS.

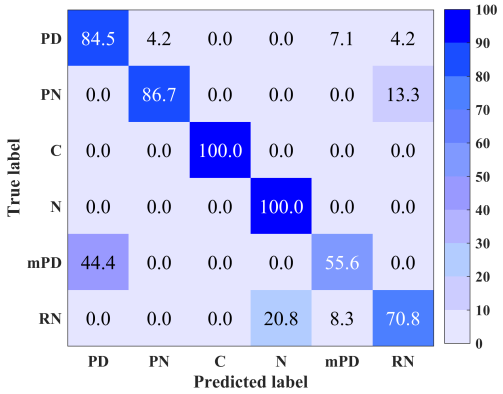

Figure 12: Confusion matrix of Site 1

5.3.2. Case 2

In this case the MCSVM was trained/tested using the ten fold cross-validation approach on a dataset that contains a mix of all the data events (7) acquired from all sites (10). A classification accuracy of 87% was achieved in this case. The drop in accuracy is realistic as the MCSVM task becomes more challenging when classifying a larger number of events. However, this may be regarded as a good performance. The confusion matrix of all events across the 10 sites is presented in Figure 16 to better understand and justify the obtained classification results. As seen, mS is the event which has the most confusions with PD, D, E, and A. PD and RN have small confusions with the other classes particularly PN, N, mPD, D, A and mS. A has confusions with PD and PN only and E has confusion of 1% with PD.

Results of the two cases show that the proposed algorithm was successful in

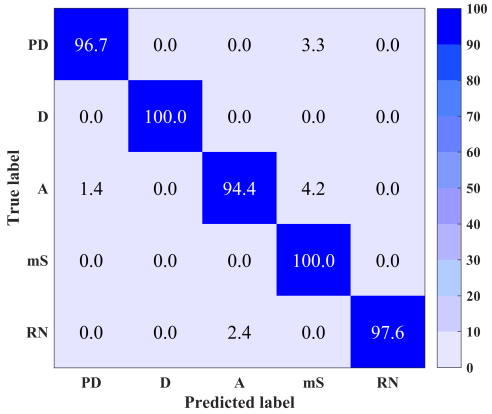

Figure 13: Confusion matrix of Site 4

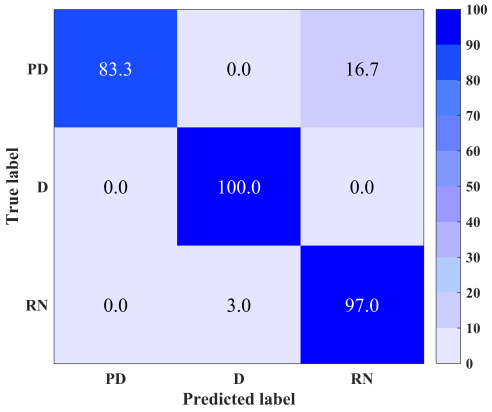

Figure 14: Confusion matrix of Site 6

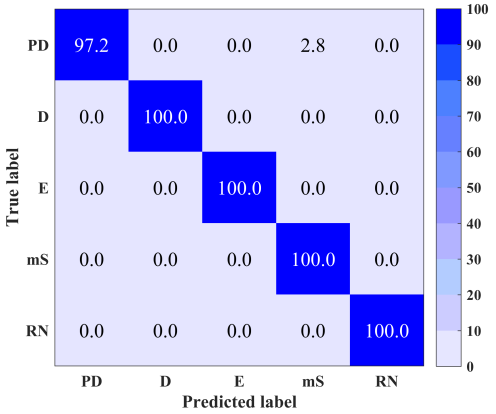

Figure 15: Confusion matrix of Site 8

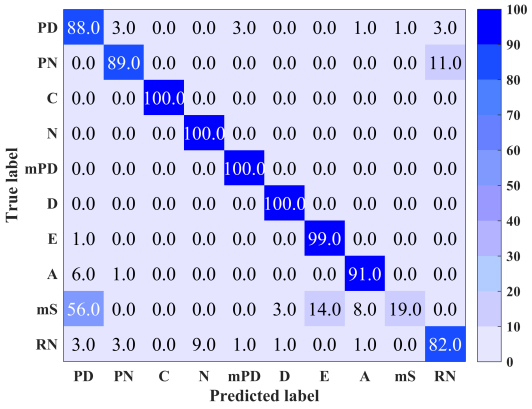

Figure 16: Confusion matrix of case 2

classification of single labelled EMI signals. This may be exploited for automatic condition assessment of high voltage assets or power plants. However, practical implementation or instrumentation of this approach may be challenging as it is heavy in computation and thus requires powerful and sophisticated computers.

6. Conclusions

This paper introduces a highly accurate feature extraction and classification algorithm that is built upon expert knowledge of electrical machine condition assessment using EMI diagnosis technique. The feature extraction was implemented to retrieve the complex difference between the time series signals of each discharge source and in order to facilitate the classification process. Excellent classification accuracy was achieved within each site as well as across all the different sites. The authors plan to investigate other aspects of the signal to address the confusion issue between PD and mPD. As for now, this work may contribute in the development of an automatic condition monitoring instrument in the future for industrial application. However, computation cost of the algorithm should be taken into account. Moreover, it would be desirable to gain more confidence in the classification by training the algorithm with more instances of EMI events.

References

[1] Y. Tian, P. Lewin, A. Davies, Comparison of on-line partial discharge detection methods for hv cable joints, IEEE Transactions on Dielectrics and Electrical Insulation 9 (2002) 604–615.

[2] L. Satish, W. S. Zaengl, Artificial neural networks for recognition of 3-d partial discharge patterns, IEEE Transactions on Dielectrics and Electrical Insulation 1 (2) (1994) 265–275.

[3] F. Kreuger, Industrial High Voltage: 4. Coordinating, 5. Testing, 6. Measuring, Delft University Press, Delft, The Netherlands, 1992.

[4] G. Robles, E. Parrado-Hernández, J. Ardila-Rey, J. M. Martínez-Tarifa, Multiple partial discharge source discrimination with multiclass support vector machines, Expert Systems with Applications 55 (2016) 417 – 428.

[5] J. E. Timperley, J. M. Vallejo, Condition assessment of electrical apparatus with emi diagnostics, IEEE Transactions on Industry Applications 53 (1) (2017) 693–699.

[6] W. J. K. Raymond, H. A. Illias, A. H. A. Bakar, H. Mokhlis, Partial discharge classifications: Review of recent progress, Measurement 68 (2015) 164 – 181.

[7] M. Wu, H. Cao, J. Cao, H. L. Nguyen, J. B. Gomes, S. P. Krishnaswamy, An overview of state-of-the-art partial discharge analysis techniques for condition monitoring, IEEE Electrical Insulation Magazine 31 (6) (2015) 22–35.

[8] M. Mondal, G. Kumbhar, Detection, measurement, and classification of partial discharge in a power transformer: Methods, trends, and future research, IETE Technical Review 0 (0) (2017) 1–11.

[9] T. Hong, M. T. C. Fang, Detection and classification of partial discharge using a feature decomposition-based modular neural network, IEEE Transactions on Instrumentation and Measurement 50 (5) (2001) 1349–1354.

[10] S. C. Oliveira, E. Fontana, Optical detection of partial discharges on insulator strings of high-voltage transmission lines, IEEE Transactions on Instrumentation and Measurement 58 (7) (2009) 2328–2334.

[11] I. Búa-Núñez, J. E. Posada-Román, J. Rubio-Serrano, J. A. Garcia-Souto, Instrumentation system for location of partial discharges using acoustic detection with piezoelectric transducers and optical fiber sensors, IEEE Transactions on Instrumentation and Measurement 63 (5) (2014) 1002–1013.

[12] W. M. F. Al-Masri, M. F. Abdel-Hafez, A. H. El-Hag, A novel bias detection technique for partial discharge localization in oil insulation system, IEEE Transactions on Instrumentation and Measurement 65 (2) (2016) 448–457.

[13] W. M. F. Al-Masri, M. F. Abdel-Hafez, A. H. El-Hag, Toward high-accuracy estimation of partial discharge location, IEEE Transactions on Instrumentation and Measurement 65 (9) (2016) 2145–2153.

[14] N. D. Jacob, W. M. Mcdermid, B. Kordi, On-line monitoring of partial discharges in a hvdc station environment, IEEE Transactions on Dielectrics and Electrical Insulation 19 (3) (2012) 925–935.

[15] G. Robles, M. Sánchez-Fernández, R. A. Sánchez, M. V. Rojas-Moreno, E. Rajo-Iglesias, J. M. Martínez-Tarifa, Antenna parametrization for the detection of partial discharges, IEEE Transactions on Instrumentation and Measurement 62 (5) (2013) 932–941.

[16] J. E. Timperley, Detection of insulation deterioration through electrical spectrum analysis, in: 1983 EIC 6th Electrical/Electronical Insulation Conference, Chicago, USA, 1983, pp. 60–64.

[17] J. E. Timperley, J. M. Vallejo, A. Nesbitt, Trending of emi data over years and overnight, in: 2014 IEEE Electrical Insulation Conference (EIC), Philadelphia, USA, 2014, pp. 176–179.

[18] J. E. Timperley, Audio spectrum analysis of emi patterns, in: 2007 Electrical Insulation Conference and Electrical Manufacturing Expo, Nashville, USA, 2007, pp. 39–41.

[19] T. K. Abdel-Galil, R. M. Sharkawy, M. M. A. Salama, R. Bartnikas, Partial discharge pattern classification using the fuzzy decision tree approach, IEEE Transactions on Instrumentation and Measurement 54 (6) (2005) 2258–2263.

[20] K. Yanbin Xie, J. Tang, Q. Zhou, Feature extraction and recognition of uhf partial discharge signals in gis based on dual-tree complex wavelet transform, European Transactions on Electrical Power 20 (5) (2010) 639–649.

[21] D. Evagorou, A. Kyprianou, P. L. Lewin, A. Stavrou, V. Efthymiou, A. C. Metaxas, G. E. Georghiou, Feature extraction of partial discharge signals using the wavelet packet transform and classification with a probabilistic neural network, IET Science, Measurement Technology 4 (2010) 177–192.

[22] R. Hussein, K. B. Shaban, A. H. El-Hag, Robust feature extraction and classification of acoustic partial discharge signals corrupted with noise, IEEE Transactions on Instrumentation and Measurement 66 (3) (2017) 405–413.

[23] J. E. Timperley, D. Buchanan, J. M. Vallejo, Electric generation condition assessment with electromagnetic interference analysis, IEEE Transactions on Industry Applications PP (99) (2017) 1–1.

[24] I. Mitiche, G. Morison, A. Nesbitt, P. Boreham, B. G. Stewart, Classification of partial discharge emi conditions using permutation entropy-based features, in: 2017 25th European Signal Processing Conference (EUSIPCO), 2017, pp. 1375–1379.

[25] C. V. Maughan, Electromagnetic interference (emi) testing of electrical equipment, in: 2011 Electrical Insulation Conference (EIC)., 2011, pp. 340–344.

[26] J. Stein, Assessment of partial discharge and electromagnetic interference on-line testing of turbine-driven generator stator winding insulation systems, `www.rpi.edu/ nelsoj/epri.pdf` (March 2003).

[27] J. E. Timperley, Comparison of pda and emi diagnostic measurements [for machine insulation], in: Conference Record of the the 2002 IEEE International Symposium on Electrical Insulation, Boston,USA, 2002, pp. 575–578.

[28] Cispr/cis/a - radio-interference measurements and statistical methods (2015).

[29] M. Chai, Y. H. M. Thayoob, P. Ghosh, A. Z. Sha'ameri, M. A. Talib, Identification of different types of partial discharge sources from acoustic emission signals in the time-frequency representation, in: Power and Energy Conference, 2006. PECon '06. IEEE International, Putrajaya, Malaysia, 2006, pp. 50–585.

[30] G. Yu, Y. Zhou, General linear chirplet transform, Mechanical Systems and Signal Processing 70–71 (2016) 958 – 973.

[31] N. Agera, S. Chapaneri, D. Jayaswal, Exploring textural features for automatic music genre classification, in: 2015 International Conference on Computing Communication Control and Automation, 2015, pp. 822–826.

[32] W. Yang, S. Krishnan, Combining temporal features by local binary pattern for acoustic scene classification, IEEE/ACM Transactions on Audio, Speech, and Language Processing 25 (6) (2017) 1315–1321.

[33] M. Esfahanian, H. Zhuang, N. Erdol, Using local binary patterns as features for classification of dolphin calls, The Journal of the Acoustical Society of America 134 (1) (2013) EL105–EL111.

[34] T. Ahohen, A. Hadid, M. Pietikainen, Face recognition with local binary patterns, in: 8th European Conference on Computer Vision, Prague, Czech Republic, 2004, pp. 469–481.

[35] Y. Huang, X. Zheng, Spectral decomposition using general linear chirplet transform, in: SEG International Exposition and Annual Meeting, Houston, USA, 2017, pp. 2164–2168.

[36] T. Ojala, M. Pietikainen, T. Maenpaa, Multiresolution gray-scale and rotation invariant texture classification with local binary patterns, IEEE Transactions on Pattern Analysis and Machine Intelligence 24 (7) (2002) 971–987.

[37] Y. Costa, L. Oliveira, A. Koerich, F. Gouyon, J. Martins, Music genre classification using {LBP} textural features, Signal Processing 92 (11) (2012) 2723 – 2737.

[38] D. Battaglino, L. Lepauloux, L. Pilati, N. Evans, Acoustic context recognition using local binary pattern codebooks, in: 2015 IEEE Workshop on Applications of Signal Processing to Audio and Acoustics (WASPAA), New York, USA, 2015, pp. 1–5.

[39] M. Topi, O. Timo, P. Matti, S. Maricor, Robust texture classification by subsets of local binary patterns, in: in Proceedings of the 15th International Conference on Pattern Recognition, Barcelona, Spain, 2000, pp. 947–950.

[40] V. Vapnik, The Nature of Statistical Learning Theory, Springer, Red Bank, NJ, 1995.

[41] C. Bishop, Pattern Recognition and Machine Learning, Springer, Cambridge, UK, 2006.

[42] B. R. K. N. S. G. Lesniak JM., Hupse R., Comparative evaluation of support vector machine classification for computer aided detection of breast masses in mammography, Physics in Medicine and Biology 57 (2012) 2560 – 2574.

[43] M. Boardman, T. Trappenberg, A heuristic for free parameter optimization with support vector machines, in: International Joint Conference on Neural Networks, Vancouver, Canada, 2006, pp. 1337–1344.

[44] A. Widodo, B.-S. Yang, Support vector machine in machine condition monitoring and fault diagnosis, Mechanical Systems and Signal Processing 21 (6) (2007) 2560 – 2574.

[45] C.-W. Hsu, C.-J. Lin, A comparison of methods for multiclass support vector machines, IEEE Transactions on Neural Networks 13 (2) (2002) 415–425.

[46] J. E. Timperley, Generator condition assessment through emi diagnostics, in: ASME 2008 Power Conference, 2008, pp. 349–354.

[47] K. M. Ting, Confusion Matrix, Springer US, Boston, MA, 2010, pp. 209–209.